

Long-Term Solar Energy Storage under Ambient Conditions in a MOF-Based Solid-Solid Phase Change Material

Kieran Griffiths¹, Nathan R. Halcovitch¹, John M. Griffin^{1,2*}

1. Department of Chemistry, Lancaster University, Lancaster, LA1 4YB, UK

2. Materials Science Institute, Lancaster University, Lancaster, LA1 4YB, UK

ABSTRACT: This paper describes the demonstration of a metal-organic framework (MOF) containing photoswitches within the pores as a hybrid solar thermal fuel (STF) and solid-solid phase change material (ss-PCM). A series of azobenzene-loaded metal-organic frameworks were synthesised with the general formula $Zn_2(BDC)_2(DABCO)(AB)_x$ (BDC = 1,4-benzenedicarboxylate, DABCO = 1,4-diazabicyclo[2.2.2]octane, AB=azobenzene; where $x = 1.0, 0.9, 0.5, 0.3$), herein named $1\supset AB_{1.0}$, $1\supset AB_{0.9}$, $1\supset AB_{0.5}$, $1\supset AB_{0.3}$ respectively. X-ray powder diffraction, solid-state NMR and DFT calculations were used to explore in detail the structural changes of the host framework that take place upon loading with the AB guest molecules. Differential scanning calorimetry measurements reveal a reversible phase change which is absent from the evacuated framework. Upon irradiation with 365 nm light, 40% of the AB guests converted from the *trans* to the higher-energy *cis* isomeric form in $1\supset AB_{1.0}$. The energy stored within the metastable *cis* isomers is released upon heating and balances the endotherm associated with the phase transition. However, the exotherm associated with the phase transition is retained upon cooling, resulting in a net energy release over a full heating-cooling cycle. The maximum energy density is observed for the fully-loaded composite $1\supset AB_{1.0}$ which releases 28.9 J g^{-1} . In addition, the *cis*-AB guests in this composite showed negligible thermal reconversion during four months at ambient temperature, with an estimated energy storage half-life of 4.5 years. Further development of MOF-based STF-ss-PCMs could lead to applications for solar energy conversion and storage, and thermal management.

1. INTRODUCTION

The development of technologies for thermal energy storage and management is crucial to support the global move towards renewable energy sources. Phase-change materials (PCMs) have the potential to store unwanted thermal energy thus providing passive cooling, and this energy can be released later for heating applications. PCMs are in general low cost, have tuneable operating temperature intervals and often have high energy storage density.¹⁻⁴ Solid-solid PCMs (ss-PCMs) are particularly sought-after because of their potential for high volumetric energy density and also because they avoid the complications of large changes in physical properties such as volume expansion, vapour pressure increases, leakage and undesired surface reactions that can be associated with solid-liquid PCMs.⁵⁻⁸ A variety of different materials have been demonstrated as solid-solid PCMs, but recent reports are predominantly focused on polyurethanes⁹⁻¹¹ or copolymerisation strategies based on either polyurethane¹²⁻¹⁵ or polyethylene glycol.¹⁶⁻²⁰ However, a common feature of most PCMs is the requirement to maintain the material at elevated temperature while energy is stored. This requirement limits the application of PCMs for long-term energy storage due to the need for constant energy input, even where effective thermal insulation is used.

An alternative technology that is well suited for long-term storage of thermal energy is solar thermal fuels

(STFs).^{21,22} In STFs, solar energy is stored through light-induced changes in the structures of molecular photoswitches to a metastable state, and the stored energy is released in the form of heat when the photoswitches undergo reconversion to the ground-state structure. The photoswitch is chosen such that the metastable form has an appropriately long half-life under ambient conditions and thus the energy can be stored for long periods and released when desired through the application of a small light or heat trigger. Several classes of molecule have been examined for use as STF materials recently such as anthracenes,²³ norbornadienes²⁴⁻²⁷ and azobenzene (AB) derivatives.^{21,28-32} In a landmark example, AB molecules were templated onto carbon nanotubes and this arrangement was shown to achieve volumetric energy density similar to lithium ion batteries.^{33,34}

In principle, it should be possible to combine the properties of ss-PCMs and STFs to design hybrid materials that can store solar energy for long periods at ambient temperatures and release it on demand as heat. Indeed, the concept of optical regulation of PCMs has been demonstrated previously whereby AB derivatives were used to trigger solidification in liquid-solid PCMs.³⁵ However, for solid-solid systems, a key challenge is that the photochemical conversion between isomers in the solid-state is usually prevented due to dense crystalline packing or steric effects. A

possible solution is to incorporate the molecular photoswitches within a porous structure such that they are confined but still have sufficient steric freedom to isomerise. Metal-organic frameworks (MOFs) are one class of porous materials ideally suited to host photo-switchable guest molecules and they have the inherent porosity required to provide a well-defined void space where photoswitches can isomerise. Furthermore, certain MOFs demonstrate solid-solid phase transitions^{36,37} often these transitions are referred to as 'breathing' because they involve a change in the pore volume. Typically breathing is induced upon guest-absorption into the pores of the material, however, in some cases it is induced thermally, raising the possibility of exploiting this for energy storage applications. Furthermore, since framework breathing significantly changes the space available within the pores, this phenomenon could be exploited to control or trigger isomerisation of guest species where significant changes in molecular geometry are required.

One example of a breathable MOF is $[Zn^{II}_2(BDC)_2(DABCO)]$ (BDC = 1,4-benzenedicarboxylate, DABCO = 1,4-diazabicyclo[2.2.2]octane (**1**),³⁷⁻⁴⁰ where 2D layers are formed by paddle wheels composed of divalent metal cations, and are bridged by BDC linkers. The layers are pillared by DABCO to form a 3D framework. **1** has been previously loaded with photochromic molecules, including AB,⁴¹ dithienylethene,⁴² and 2-phenylazopyridine.⁴³ Upon loading with *trans*-AB, Kitagawa and coworkers⁴¹ showed that there is a guest-induced contraction of the unit-cell and a distortion of the 2D grid. Exposure to UV light results in a guest-induced structural expansion caused by isomerisation of a proportion of *trans*-AB to the metastable *cis* isomer. Up to 80% of the initial light-induced population of the *cis* isomer was retained after 30 days at ambient temperature, suggesting promising properties for long term energy storage, comparable to the most stable AB-based STFs.²¹ The energy difference between *cis* and *trans*-AB isomers is approximately 50 kJ mol⁻¹.^{32,33} Assuming a loading of one AB molecule per formula unit of **1**, the theoretical energy density of this system may be up to 66 J g⁻¹ depending on the photostationary state achieved. However, the structures and behaviour of AB within the pores of **1** are not well understood and the thermal properties resulting from the photoswitching of the guest species and breathing of the framework have not yet been studied.

In this work, we report the synthesis and detailed characterisation of the structural and thermal properties of a series MOF-AB composites with different loading levels of AB: $Zn_2(BDC)_2(DABCO)(AB)_x$ (where $x = 1.0, 0.9, 0.5, 0.3$), herein named $1\supset AB_{1.0}$, $1\supset AB_{0.9}$, $1\supset AB_{0.5}$, $1\supset AB_{0.3}$ respectively. Solid-state NMR and X-ray powder diffraction (XRPD) have been used in tandem to understand the structural changes the $1\supset AB_x$ composites undergo as a function of loading and when exposed to UV light. DSC has also been used to quantify the onset temperature and thermal energy associated with a structural phase transition, and the thermally-triggered reconversion from *cis*- to *trans*-AB in these systems. We find that this model system exhibits a thermal energy density comparable to other inorganic ss-

PCMs, demonstrating that with further development MOF-based ss-PCMs may be viable candidates for long-term solar thermal energy storage and thermal management.

2. EXPERIMENTAL SECTION

Synthesis of 1. All reagents were obtained from Fluorochem and used without further purification. $Zn_2(BDC)_2(DABCO)$ (**1**) was synthesised according to previously reported synthetic procedures.⁴⁴ $Zn(NO_3)_2 \cdot 6H_2O$ (0.5 g, 1.68 mmol) was sonicated in *N,N*-dimethylformamide (DMF, 20 mL) until fully dissolved, 1,4-dibenzendicarboxylic acid (0.28 g, 1.68 mmol) and DABCO (0.093 g, 0.84 mmol) were then added. The reactant solution was placed in a stainless-steel autoclave (Parr) with a Teflon lining with a 50 mL capacity. The solution was heated at 120 °C for 48 h and left to cool to room temperature. The colourless crystals were collected via vacuum filtration and washed with DMF (3 x 30 mL) before drying under ambient conditions.

Loading of 1 with AB. Samples of **1** were loaded with AB using a previously published melt-infiltration procedure.⁴¹ As-prepared samples of **1** were first heated at 120 °C under vacuum for 24 h to remove DMF solvent molecules. 300 mg of the evacuated material was then mixed with a defined mass of *trans*-AB and heated at 120 °C for between 1 - 6 h. Excess AB was removed by heating at 120 °C under vacuum for between 1 - 6 h.

Quantification of loading level by UV-Vis spectroscopy. UV-Vis data was collected on a Cary 60 UV/VIS spectrophotometer with a quartz cell (3 mL) within a 200-600 nm range. A calibration curve with known concentrations of *trans*-AB was constructed (S₂). AB was extracted from $1\supset AB_x$ (50 mg) using MeOH (10 mL x 4) and the filtrate was collected. The orange filtrate was combined, and the solution was diluted to a volume of 50 mL.

Quantification of loading level by acid digestion and ¹H NMR spectroscopy. 10 mg of $1\supset AB_x$ was suspended in DCI (1.5 mL) and DMSO-*d*₆ (1.5 mL) and placed in a stainless-steel autoclave (Parr) with a Teflon lining with a 50 mL capacity. The suspension was heated for 12 h at 100 °C to yield a transparent solution. A Bruker Avance III 400 NMR spectrometer with a 5 mm ¹H-X broadband observe probe was used to collect ¹H NMR data. The ¹H NMR spectrum of the solution was taken and the ratio between DABCO, BDC and *trans*-AB was determined from the integration of characteristic ¹H resonances.

Photostationary state determination of irradiated $1\supset AB_x$ composites. 25 mg of $1\supset AB_x$ was suspended in MeOH-*d*₄ (0.5 mL) in an Eppendorf and shaken. The Eppendorf was centrifuged to separate the solid from the solution. A Bruker Avance III 400 NMR spectrometer with a 5 mm ¹H-X broadband observe probe was used to collect ¹H NMR data. The population ratio of *trans*-AB and *cis*-AB isomers was determined from integration of *trans* and *cis* resonances in the ¹H NMR spectrum based on literature values. The remaining solid was digested in DCI (1.5 mL)

and DMSO- d_6 (1.5 mL) and placed in a stainless-steel autoclave (Parr) with a Teflon lining with a 50 mL capacity. The suspension was heated for 12 h at 100 °C to yield a transparent solution. The ^1H NMR spectrum of the solution was taken, and no residual *trans*-AB or *cis*-AB resonances were detected. The process was repeated three separate times and *cis/trans* ratios were consistent.

UV light irradiation procedure. Samples were irradiated with an OmniCure LX5 LED Head with a power of 425 mW and a 3 mm focusing lens. 50 mg of finely ground 1DAB_x was spread homogeneously over a microscope slide. The powder was spread into a circle with a 1 cm radius which was approximately 0.5 mm thick so that irradiation was approximately uniform. The slide was placed under 365 nm light at a distance of 5 cm. The beam was set to 50% intensity and exposed for a fixed duration. The sample was incrementally agitated to allow all particulates to be exposed to the beam.

Solid-state NMR. Solid-state NMR experiments were performed on Bruker Avance III HD spectrometer operating at magnetic field strength of 16.4 T, corresponding to ^1H and ^{13}C Larmor frequencies of 700 and 176 MHz, respectively. Spectra are referenced relative to tetramethylsilane (^{13}C / ^1H) using the CH_3 ($^1\text{H} = 1.1$ ppm; $^{13}\text{C} = 20.5$ ppm) resonances of *L*-alanine as a secondary reference. ^{13}C NMR spectra were recorded at a magic-angle spinning (MAS) rate of 16.0 kHz using cross polarization (CP) to transfer magnetization from ^1H with a contact time of 3 ms. The CP pulse was ramped linearly from 70 – 100% power. ^1H heteronuclear decoupling using two-pulse phase modulation (TPPM)⁴⁵ with a pulse length of 4.8 μs and a radiofrequency field strength of 100 kHz was applied during acquisition. Spectra are the sum of 512 transients separated by a recycle interval of 10 s. The sample temperature in variable-temperature experiments was calibrated using $\text{Pb}(\text{NO}_3)_2$.⁴⁶

XRPD. X-ray powder diffraction (XRPD) patterns were measured with a Rigaku SmartLab X-ray diffractometer with a 9 kW rotating anode Cu-source equipped with a high-resolution Vertical θ/θ 4-Circle Goniometer and D/teX-ULTRA 250 High-Speed Position-Sensitive Detector System in reflectance mode. The system was configured with parallel-beam optics and a Ge(220) 2 bounce monochromator on the incident side. Powdered solid samples were prepared on glass slides. The measurements were performed as $\theta/2\theta$ scans with a step size of 0.01 degrees.

Density Functional Theory Calculations. First-principles calculations of NMR parameters were carried out under periodic boundary conditions using the CASTEP code⁴⁷ employing the gauge-including projector augmented wave (GIPAW) algorithm.⁴⁸ Prior to calculation of the NMR parameters, structures were fully geometry optimised, with all atomic positions to vary. For calculations on guest-free frameworks, the input atomic coordinates were taken from literature structures with the guest molecule atoms deleted.⁷ The structures were then optimized while keeping the unit cell parameters fixed to the experimental values. Atomic coordinates for optimized structures are given as cif files in Supporting Information. Single-molecule calculations were carried out in a $20 \times 20 \times 20$ Å cell with fixed

cell parameters to ensure molecules remained isolated from periodic replicas. The initial molecular models for these calculations were constructed using GaussView software before being optimized within CASTEP. Full details are given in Supporting Information (DFT Calculation Details).

2. RESULTS AND DISCUSSION

3.1. Guest-induced breathing of 1DAB_x . To explore the structural changes upon incorporation of AB guests within the pores of **1**, a series of samples was synthesised with different loading levels of *trans*-AB (S_1). Samples are hereafter referred to as 1DAB_x where x represents the stoichiometric ratio of AB molecules to the formula unit of **1**. A value of $x = 1$ is equivalent to one AB molecule per pore. The loading level was varied by changing the mass of AB relative to the mass of **1** used in the melt infiltration procedure, and was quantified by solvent extraction of the guests followed by UV-Vis spectroscopy (S_2 and S_3), as well as by digestion followed by ^1H NMR (S_2).

Figure 1 shows XRPD patterns of 1DAB_x samples. The data for guest-free **1** is fully consistent with the previously reported large-pore (*lp*) tetragonal ($P4/mmm$) structure (S_4 -5).⁴⁴ For the lowest loading of *trans*-AB, $1\text{DAB}_{0.3}$, profile fitting shows the tetragonal ($P4/mmm$) symmetry is retained, however reflections of a new phase also emerge. These are consistent with the orthorhombic ($Cmmm$) space group previously reported by Yanai *et al.* (S_5),⁴¹ which arises from guest-induced breathing of the structure. The contraction of the framework around the *trans*-AB guest species distorts the *lp* 2D square grid resulting in a narrow-pore (*np*) 2D rhombic grid with reduced specific volume.^{41,43} The co-existence of the tetragonal and orthorhombic phases suggests that the guest-induced breathing is a local effect and the tetragonal *lp* structure is maintained in regions of the structure containing empty pores. As the loading level is increased, the intensity of the orthorhombic reflections increase, and as saturation is approached in $1\text{DAB}_{0.9}$, the tetragonal *lp* phase is no longer observed. However, for $1\text{DAB}_{0.9}$, in addition to the dominant orthorhombic *np* phase, weak reflections

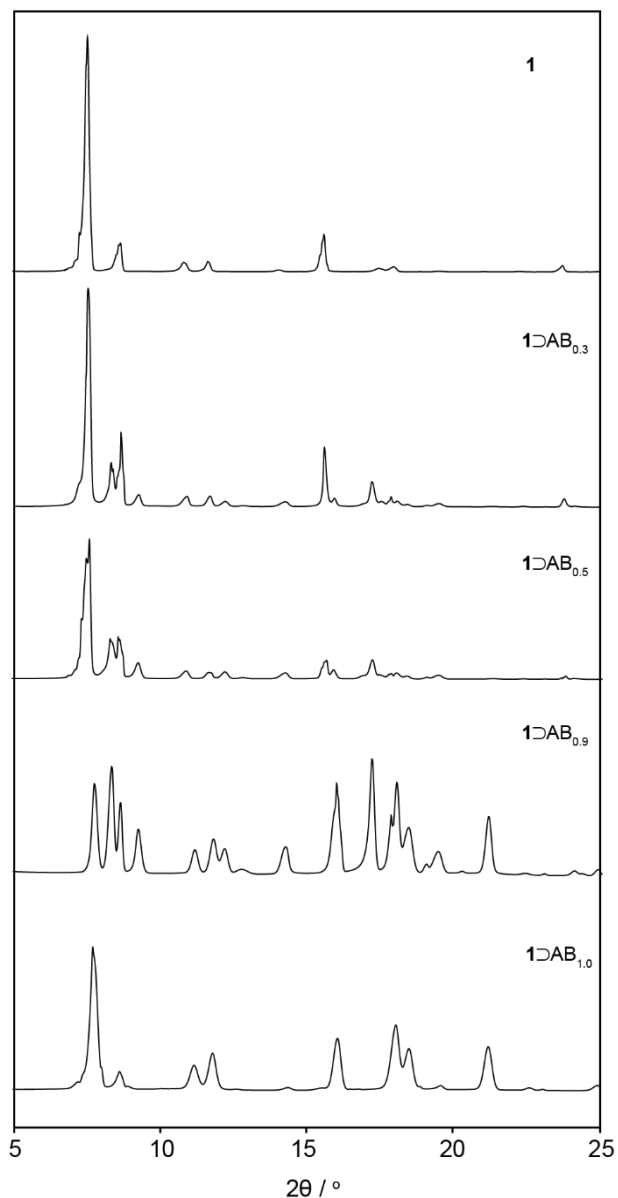


Figure 1. XRPD patterns of 1DAB_x composites with loading levels between 0 - 1.

corresponding to a new phase are observed. For the fully-loaded sample, $1\text{DAB}_{1.0}$, the XRPD pattern is dominated by this new phase. A Le Bail fitting analysis showed good agreement with the tetragonal space group I_4/mcm , which is the same as that adopted for **1** loaded with DMF (1DDMF) (S5). The unit cell dimensions have increased with $a = b = 15.03 \text{ \AA}$ and $c = 19.28 \text{ \AA}$, with a volume of 4355.9 \AA^3 . However, there is a contraction, per formula unit, of the $a = b$ cell length from 10.98 \AA (**1**) to 10.63 \AA ($1\text{DAB}_{1.0}$), whereas the c cell length remains at 9.65 \AA . This indicates that the BDC ligands (which are aligned along the $a = b$ axes) distort due to the contraction of the pore around the occluded *trans*-AB molecules. Indeed, such distortion is observed for **1** loaded with DMF (1DDMF) whereby the ligands undergo significant bending around the guest molecules resulting in twisting of the Zn_2 paddle wheel unit.⁴⁴

The volume per formula unit for $1\text{DAB}_{1.0}$ (1089.0 \AA^3) is reduced compared to that for guest-free **1** (1162.6 \AA^3); however, it is larger than the orthorhombic *np* phase (1042.0 \AA^3) observed for $1\text{DAB}_{0.3}$ and $1\text{DAB}_{0.9}$. The volume per formula unit for $1\text{DAB}_{1.0}$ is very close to 1DDMF (1091.8 \AA^3), which is consistent with the contraction of the pores around the guest molecules.⁴⁴

The observation of a new tetragonal *np* phase for $1\text{DAB}_{1.0}$ contradicts previous measurements by Yanai *et al.* who reported the orthorhombic space group for the fully-loaded structure. However, we note that this new phase is only observed at very high loading above a molar ratio of 0.9 *trans*-AB molecules per formula unit. Furthermore, through careful quantification of the loading level as described above, it was found that the vacuum treatment step in the loading procedure reduced the final loading level (S6). This step is necessary to remove excess *trans*-AB that is not occluded within the pores, but was also found to partially remove *trans*-AB molecules from within the pores. In order to achieve a fully loaded sample with a molar ratio of 1.0, the vacuum treatment time was reduced from six hours used in the previous work to three hours. This was still found to be sufficient to remove the excess *trans*-AB as evidenced by the absence of crystalline *trans*-AB reflections in XRPD pattern (S7). We also note that Yanai *et al.* used a gas phase loading method whereas $1\text{DAB}_{1.0}$ in this study was loaded by melt infiltration. It may be possible that the loading method can affect the organization of AB molecules inside the pores, leading to structural differences at high loading level.

The shift to the new tetragonal *np* phase at high loading suggests that some global reorganisation of the structure is necessary to accommodate *trans*-AB at this level. It is noteworthy that there is a mismatch between the length of the *trans*-AB molecule (11.3 \AA) and the c axis pore dimension **1** (9.65 \AA). If the *trans*-AB molecules orient along this axis (which defines the main pore channel within the structure) it would not be possible to accommodate a single *trans*-AB molecule in each pore. Therefore, some degree of reorganisation and partial stacking of *trans*-AB molecules along the c -axis may be necessary to reach the highest loading level, which in turn, leads to a partial expansion of the unit cell parameters and overall unit cell volume compared to the orthorhombic structure observed for lower loading levels.

To gain further insight into the guest-induced breathing of **1**, ^{13}C CPMAS NMR spectra were recorded (Figure 2). For guest-free **1**, four resonances corresponding to the crystallographically-distinct BDC and DABCO carbon sites are observed. The chemical shifts for carbons within the DABCO group are averaged by fast rotation around the central $\text{N} \dots \text{N}$ axis to give a single resonance at 47.3 ppm .⁴⁹ The carbonyl and quaternary ring carbons are observed at 171.0 and 137.4 ppm , respectively. The ring CH at 127.9 ppm is significantly broadened; we attribute this to motional broadening due to kHz-timescale ring-flipping dynamics which has previously been characterised by ^2H NMR on deuterated samples.⁵⁰ Indeed, a spectrum recorded at $80 \text{ }^\circ\text{C}$ (where the timescale of the ring flipping dynamics should

be significantly increased) displayed pronounced motional narrowing of this resonance (S8). As the structure is loaded with AB, additional resonances corresponding to the guest species are observed, while chemical shift changes of the BDC and DABCO groups arise due to the guest-induced breathing. Considering the framework resonances, for $1\supset\text{AB}_{0.3}$, the transition to the np orthorhombic phase is signified by the appearance of a new carbonyl resonance at 174.1 ppm and a “shoulder” on the DABCO resonance at 47.6 ppm. DFT chemical shift calculations for an empty framework constrained to the experimental unit cell dimensions of the orthorhombic np phase confirms that these changes are due to the distortion of the Zn_2 paddle wheel motifs to which the carbonyl and DABCO groups coordinate (S9). For $1\supset\text{AB}_{0.5}$, the relative intensities of the carbonyl and DABCO resonances associated with the orthorhombic phase increase, reflecting the increased proportion of the framework that adopts this structure. As the loading level is increased further for $1\supset\text{AB}_{0.9}$, the 47.6 ppm DABCO resonance saturates and a new resonance is observed at 48.4 ppm, consistent with the onset of the structural transition to the np tetragonal phase. This higher chemical shift is very similar to that observed for $1\supset\text{DMF}$ at 47.8 ppm (S10), suggesting that it arises from the twisting of the Zn_2 paddle wheel motifs due to the bending of the BDC linkers. In addition, a new carbonyl resonance is observed at 170.7 ppm which is slightly shifted from the carbonyl shift for guest-free **1** and is also similar to the carbonyl chemical shift for $1\supset\text{DMF}$ at 170.6 ppm (S10). DFT chemical shift calculations for an empty framework constrained to the distorted tetragonal np structure, with unit cell dimensions of $1\supset\text{AB}_{1.0}$, also agree with the experimental shifts (S9). For the fully-loaded sample $1\supset\text{AB}_{1.0}$, the carbonyl resonance corresponding to the orthorhombic structure is no longer observed, confirming that the structure has fully converted to the tetragonal np phase. However, the DABCO resonance remains split with peaks of equal intensity at 47.6 and 48.4 ppm. This splitting is mirrored in the ^1H MAS NMR spectrum which also shows two DABCO resonances of equal intensity (S11). This suggests the ordering of AB molecules within the pores of the fully-loaded structure results in a subtle lowering of the local symmetry of the DABCO groups which is not resolved in the XRPD data.

Considering the AB guest molecules, for the low-loaded samples $1\supset\text{AB}_{0.3}$ and $1\supset\text{AB}_{0.5}$, resonances corresponding to the C-N carbons and ring carbons are centred around 153 and 120 ppm, respectively. The splitting of these resonances suggests two crystallographically-inequivalent molecular conformations within the pores, which is consistent with the two DABCO resonances. For $1\supset\text{AB}_{0.9}$ and $1\supset\text{AB}_{1.0}$, the transition to the tetragonal np structure is accompanied by changes in the chemical shifts of these sites, further suggesting that the AB molecules rearrange within the pores to achieve full loading of the structure. Interestingly, a DFT chemical shift calculation on an isolated molecule gives poor agreement with the observed shifts, with shifts for the C2 carbons expected at 110 ppm where none are observed experimentally (S12 and S13). However, averaging

shifts for sites on opposite sides of the six-membered rings gives good agreement with the observed chemical shifts (Figure 2). Such averaging suggests fast rotational dynamics of the AB molecules within the pore. Indeed, a spectrum recorded at -31°C showed a pronounced broadening of the AB ring resonances, consistent with a reduction in the timescale of the motional process (S13). One possible form of motion is fast flipping of the six-membered rings around the C-N axis; however, given the dense packing of the structure it is unlikely that there is sufficient space for this to occur (S14 and S15). Another explanation for the observed averaging is fast pedal motion of the central N=N linkage, which would also have the same averaging effect. Dynamic pedal motion has been observed in crystalline azobenzenes but typically occurs on the timescale of tens of Hz at ambient temperatures,^{51,52} which is too slow to result in motional averaging (S16). For motional averaging to occur in $1\supset\text{AB}$, the pedal motion must take place on a timescale faster than approximately 10 kHz (see S16 for more details). This corresponds to a reduction in activation energy by more than 11 kJ mol⁻¹, meaning that the steric freedom must be significantly increased for the AB molecules occluded within the pores of **1** as compared to other crystalline azobenzenes.

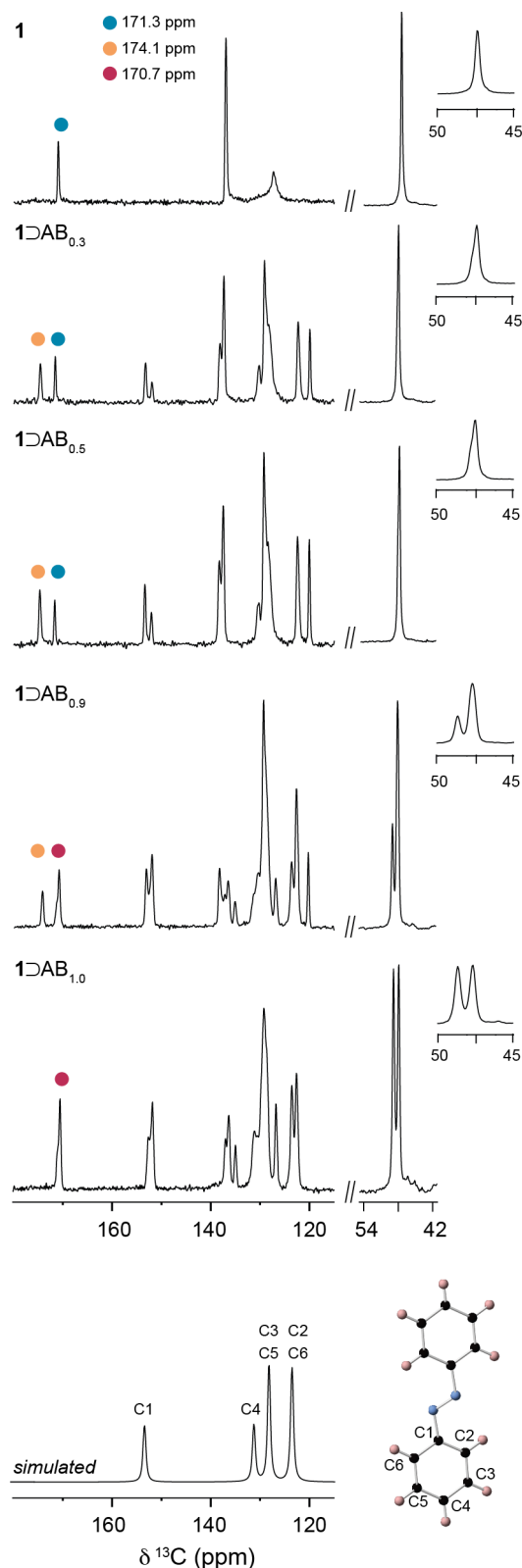


Figure 2: ^{13}C CPMAS NMR spectra of 1DAB_x composites with different loading levels. Expansions of the DABCO resonances are shown in the insets. Bottom: simulated ^{13}C NMR spectrum of a single molecule of *trans*-AB assuming rotational averaging around the N=N axis.

3.2. Thermally-driven phase changes in 1DAB_x . When guest species or functional groups are present in the pores,

the topology of **1** is well-known to undergo thermally activated, fully reversible phase transitions from the contracted *np* phase to the expanded *lp* phase with an associated phase transition enthalpy which can be observed by DSC.⁵³⁻⁵⁶ To investigate the thermal properties of 1DAB_x , cyclic DSC measurements were performed in the range 0 – 200 °C at a rate of 20 °C min⁻¹ (Figure 3, S17). For guest-free **1**, no thermal features were observed, consistent with it remaining in the tetragonal *lp* structure over the temperature range studied. For $1\text{DAB}_{0.3}$, a small endothermic phase transition is observed at 124 °C. As the loading level is increased, the onset temperature of the endotherm shifts to 162 °C and the magnitude of the endothermic enthalpy increases up to a maximum value of 21.6 kJ mol⁻¹ for $1\text{DAB}_{1.0}$.

Thermally-driven *np*-*lp* phase changes have been previously reported by Henke and coworkers for structurally analogous $[\text{Zn}(\text{fu-BDC})_2(\text{DABCO})]$ (fu = *n*-butoxy, 2-methoxyethoxy) frameworks.⁵⁴ The framework structures of these materials are identical to **1**; however, the BDC ligand is modified with alkoxy groups which act as tethered guest species resulting in contraction of the structure to the *np* form at ambient temperature. The length of the alkoxy chain was found to modulate the thermo-responsive behaviour of the *np*-*lp* phase transitions, with linear substituents of five non-hydrogen atoms having phase change enthalpies between 6.0 – 18.0 kJ mol⁻¹, whereas shorter chains exist exclusively in the *np* form and longer ones in the *lp* form. The phase transition enthalpy of 21.6 kJ mol⁻¹ for $1\text{DAB}_{1.0}$ is larger than those observed in the previous work, which may suggest that stronger interactions (*e.g.*, π - π interactions) between the guest molecules or between the guests and the framework are involved.

The cooling branches of the DSC traces show that the phase transition is fully reversible, with exotherms of very similar magnitude observed at similar temperatures. A slight hysteresis is observed, with the transitions during cooling taking place at slightly lower temperatures. Such hysteresis was also observed in DSC measurements of structurally-related frameworks undergoing reversible *np*-*lp* phase transitions.⁵⁴ However, the temperature difference between the endothermic and exothermic features reduces with reduced heating rate, confirming they arise due to the same process (S18). While the phase transitions in the 1DAB_x composites are fully reversible, when samples were held above the phase transition temperature for an extended period of time, *trans*-AB was observed to desorb from the framework pores, as evidenced by a characteristic crystallisation at 69 °C during a full heating cycle (S19). After eight minutes above the transition temperature, 19 % of the total *trans*-AB within $1\text{DAB}_{1.0}$ left the pores (S20). In such cases, the magnitude of the phase transition enthalpy on the subsequent heating-cooling cycle was reduced concomitantly. However, by optimising the heating rate and maximum sample temperature in the DSC measurements, it was possible to prevent the loss of *trans*-AB from the framework pores. TGA analysis of 1DAB_x shows that the loss of *trans*-AB is negligible between 25 – 200 °C with a scan rate of 20 °C min⁻¹ and that thermal degradation of the composite structure does not occur until 225 °C (S21). Loss

of AB from the structure was also observed for low AB loadings over extended periods of time (5 days) at ambient temperature. However, when the structure was fully loaded, no loss of AB was detected over a period of 30 weeks at ambient temperature. This suggests that the *lp* regions facilitate diffusion of AB molecules through the structure leading to their eventual desorption. For the fully-loaded sample, the global pore contraction associated with the *np* structure helps to immobilise the molecules within the pores.

VT-XRPD studies on $1\text{DAB}_{1.0}$ between 25–180 °C show that the *np* tetragonal $I4/mcm$ phase is stable up to 160 °C. At 180 °C, the orthorhombic $Cmmm$ phase is observed (equivalent to the dominant phase in $1\text{DAB}_{0.9}$ at room temperature). This may reflect the fact that the prolonged heating during the XRPD experiment leads to some loss of AB from the pores, resulting in a slightly lower loading level. Unlike previous studies on functionalized analogues of **1**, we do not see clear evidence that the thermal features observed in the DSC measurements correspond to a *np-lp* phase transition. However, the prolonged duration of the XRPD measurements compared to the DSC measurements, together with the loss of AB from the pores, may mean that short-lived structural changes are not observed. Figure 3 shows that the magnitude of the phase transition enthalpy varies approximately linearly with the mole fraction of AB in the sample. Since the *np* framework adopts different structures throughout the compositional range (*i.e.*, orthorhombic and tetragonal), this linear relationship suggests that the phase change enthalpy is dominated by framework host-guest interactions or reorientation or rearrangement of the guest molecules rather than the intrinsic change of the framework structure itself. The lower phase transition temperature of $1\text{DAB}_{0.3}$ suggests that the large regions of guest-free *lp* framework facilitate the structural change that takes place in the minority *np* regions that are present.

The thermally-induced reversible phase transition observed for 1DAB_x system gives it the properties of a ss-PCM and is reminiscent of organometallic and inorganic ss-PCMs which store and release energy via crystallographic structure transformations or order-disorder transformations.⁵⁷ The gravimetric energy density of $1\text{DAB}_{1.0}$ is 28.4 J g⁻¹, and the volumetric energy density based on the unit cell parameters of the tetragonal *np* phase equates to 33 MJ m⁻³. Both of these values are comparable to some organometallic layered perovskite SS-PCMs^{58–61} but are lower than organic polymer-based SS-PCMs which can exhibit phase transition enthalpies in excess of 100 J g⁻¹.⁶² The phase transition temperature of 162 °C for the higher loaded samples is higher than transition temperatures for organometallic layered perovskite SS-PCMs^{63–65} but significantly lower than fully inorganic metal-based SS-PCMs.⁵⁷ However, the main limitation of 1DAB_x as a SS-PCM is the loss of AB from the pores. Two of the key requirements of ss-PCMs are to be thermally stable over multiple heating cooling cycles, and to be able to store energy for extended durations above the phase transition temperature. For $1\text{DAB}_{1.0}$ the guest molecules leave the pores after an extended period above the phase transition temperature. Since pores that do not contain AB do not undergo an exothermic phase transition

upon cooling, loss of AB from the pores at high temperature reduces the amount of energy that can be recovered from the material. Therefore, this system has limited viability as a ss-PCM while the guest AB molecules are in the *trans* isomeric state.

3.3. Light-induced structural changes and energy storage in $1\text{DAB}_{1.0}$. Yanai *et al.* have previously shown that the *trans*-AB guest molecules within the orthorhombic phase of 1DAB_x exhibit photoisomerization upon exposure to UV light. To determine if photoisomerization also occurs in the more densely packed tetragonal phase, $1\text{DAB}_{1.0}$ was irradiated with 365 nm light for varying amounts of time. Subsequent solvent extraction of the guest AB molecules followed by ¹H NMR showed that photoisomerization to *cis*-AB takes place within $1\text{DAB}_{1.0}$ despite the dense packing of the molecules

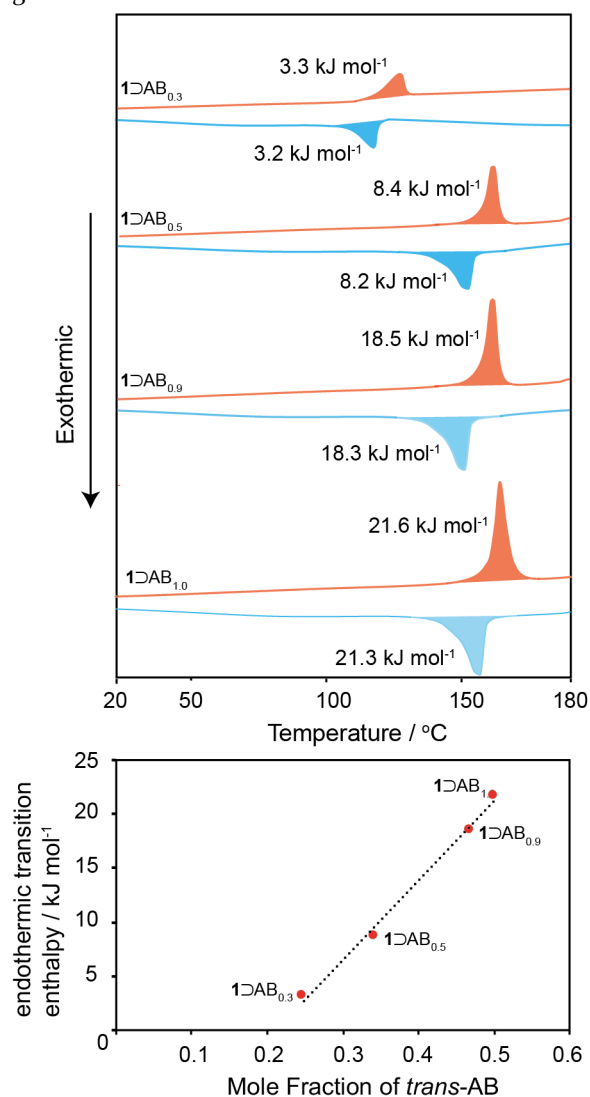


Figure 3. (a) First DSC cycles of 1DAB_x between 0 – 200 °C at 20 °C min⁻¹, with heating branches in red and cooling branches in blue. (b) Endothermic phase transition enthalpies as a function of mole fraction of AB in 1DAB_x samples. Phase transition enthalpies are derived from integration

of the endotherms observed in first heats in the DSC experiments and are expressed in terms of kilojoules per mole of sample at that composition.

(S23). This was confirmed by FTIR measurements which show the formation of a double peak characteristic of the *cis* isomer at 697 cm^{-1} . Figure 4 shows the proportion of *cis*-AB molecules measured by ^1H NMR for irradiation times between 0 – 300 minutes. The results show that a photo-stationary state (PSS) of 40% is reached after approximately 300 minutes. This is lower than the PSS of ~80% that can be achieved in solution;⁶⁶ however, additional experiments with up to 7 hours irradiation did not increase the PSS beyond this value. $1\text{DAB}_{0.9}$ and $1\text{DAB}_{0.5}$ exhibited slightly lower PSSs, while that for $1\text{DAB}_{0.3}$ was significantly reduced at 13%. This suggests expansion of the framework with AB loading level may play a role in allowing AB to photoisomerise. At the same time, for $1\text{DAB}_{1.0}$, the dense packing of AB molecules inside the pores may result in steric effects either between AB molecules or related to the framework which place an upper limit of 40% on the number of molecules that can isomerise.

XRPD measurements were also performed to monitor the structural changes that take place during UV irradiation. As the irradiation time increases, the reflections of the *np* tetragonal phase of $1\text{DAB}_{1.0}$ shift slightly and decrease in intensity and new reflections emerge (Figure 4, S24). As the fraction of *cis*-AB increases the relative intensity of the new phase also increases and after 300 minutes it dominates the XRPD pattern. The *np* tetragonal phase remains present but at a very low intensity. This suggests that the structural change is a global transformation which incorporates both the *cis* and *trans* isomers at the PSS, rather than segregation into separate *cis*- and *trans*-isomer containing domains. This also further suggests that the maximum PSS of 40% *cis*-AB is an intrinsic property of the system and is not due to incomplete light penetration, which would result in separate domains. For irradiated $1\text{DAB}_{1.0}$, the new phase was extracted, and a Le Bail fitting analysis showed good agreement with the same tetragonal space group $I4/mcm$ (S24). There is a lengthening of the $a = b$ unit cell length from 15.03 \AA to 15.41 \AA , whereas the length of the c axis remains at 19.28 \AA . Therefore irradiated $1\text{DAB}_{1.0}$, which has a unit cell volume of 4539.8 \AA^3 , remains partially contracted compared to guest-free **1**, although it is expanded in comparison to $1\text{DAB}_{1.0}$. The irradiation of the other 1DAB_x composites ($x = 0.3, 0.5$ and 0.9) also induced changes in the observed reflections (shown in Figs. S24a-d). For $1\text{DAB}_{0.9}$, profile fitting shows that the contracted $I4/mcm$ and the large pore $P4/mmm$ phases are present (S24b). The conversion of the orthorhombic phase to the large pore tetragonal phase is consistent with work by Yanai *et al.*⁴¹ Interestingly, only small reflections of the initial orthorhombic phase are retained, which may indicate a preferential switching of AB molecules and a less confined environment in the MOF pore. The emergent reflections in $1\text{DAB}_{0.3}$ and $1\text{DAB}_{0.5}$ were too small and overlapped with initial reflections to be accurately indexed.

To gain insight into the local structural changes that take place upon irradiation of $1\text{DAB}_{1.0}$, ^{13}C CPMAS NMR spectra

were recorded for samples irradiated for different durations (Figure 5a). With increasing irradiation time, the most obvious changes are observed in the DABCO region where the intensity of the 48.4 ppm resonance reduces, while that of the 47.4 ppm resonance increases (S25). The ^1H MAS NMR spectrum (S11) also shows a loss of the high-chemical shift DABCO resonance. This is consistent with the expansion of the unit cell dimensions observed by XRPD which suggests the BDC ligands in the tetragonal grid become less distorted. Such expansion would also reduce the distortion of the Zn_2 paddle wheel units leading to a chemical shift for the DABCO group closer to that of guest-free **1**. However, we note that the DABCO resonance in the 300-minute irradiated sample (47.4 ppm) is still discernibly shifted compared to guest-free **1** (47.3 ppm), suggesting that some distortion remains. Considering the aromatic region (S26), isomerisation of the AB guest molecules does not shift the BDC carbonyl resonance; however, the split quaternary carbon resonance (137.2 ppm and 136.7 ppm) gradually merges into a single resonance (137.2 ppm). Resonances corresponding to the *trans*-AB

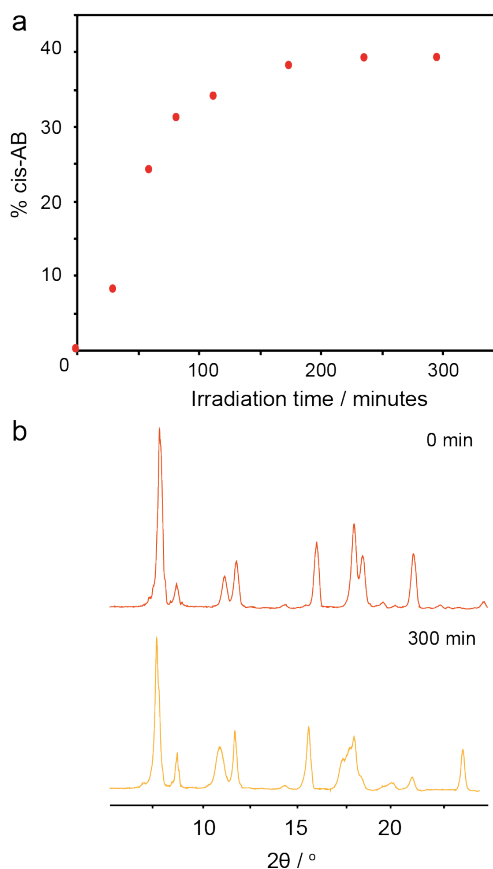


Figure 4. (a) The proportion of *cis*-AB in $1\text{DAB}_{1.0}$ as a function of irradiation time as measured by ^1H NMR. (b) Comparison of XRPD patterns of $1\text{DAB}_{1.0}$ before and after irradiation.

molecules decrease in relative intensity as they convert to the *cis*-isomer. However, no resonances characteristic of *cis*-AB are observed after 300 minutes irradiation (Figure 5b). To investigate if dynamic effects may be responsible

for the absence of these resonances, a spectrum was recorded at a lower temperature of $-31\text{ }^{\circ}\text{C}$ (Figure 5b, S27). In this spectrum, two new resonances are observed at 156.9 ppm and 118.3 ppm. A simulation whereby shifts for chemically-equivalent species are averaged shows good agreement with the experimental data (Figure 5, S28-29), suggesting that the *cis*-AB molecules are undergoing rapid rotational motion. The absence of *cis*-AB resonances at ambient temperature suggest that the timescale of the motion at this temperature broadens the resonances beyond detection. Indeed, the non-linear geometry of *cis*-AB may facilitate molecular tumbling within the pores. When the temperature is reduced to enable observation of the *cis*-AB resonances, the fact that chemically-equivalent sites are averaged shows that there is still significant conformational dynamics of the molecule within the pores including rotation of the rings around the C-N and switching of the ring orientations with respect to the central N=N bond.

Together, the XRPD and solid-state NMR data show that UV irradiation of $1\text{DAB}_{1,0}$ results in photoisomerization of the occluded AB molecules to the metastable *cis*-AB isomer, which is highly dynamic within the pores. This is accompanied by a slight expansion of

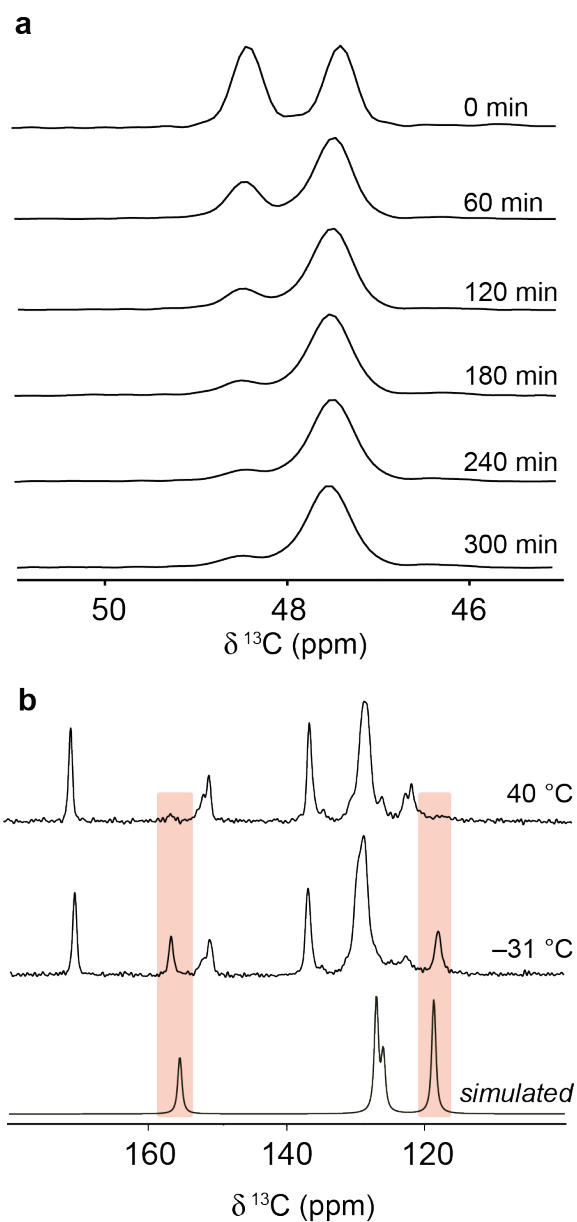


Figure 5. (a) Comparison of the DABCO region of ^{13}C CPMAS NMR spectra of $1\text{DAB}_{1,0}$ for irradiation times between 0-300 minutes. (b) ^{13}C CPMAS NMR spectra of irradiated $1\text{DAB}_{1,0}$ recorded at ambient temperature (corresponding to $40\text{ }^{\circ}\text{C}$ sample temperature due to frictional heating from MAS, top) and $-31\text{ }^{\circ}\text{C}$ (middle). A simulated ^{13}C NMR spectrum of a single molecule of *cis*-AB with averaged chemical shifts for chemically-equivalent sites to mimic the effect of molecular rotation is shown below.

the pores which can be rationalised in terms of straightening of the BDC linkers, resulting in a larger $a = b$ unit cell dimensions. This is supported by the marginal shift which the carbonyl carbon of the BDC linkers see during irradiation and the convergence of the DABCO resonance into a single resonance which resembles a structure like guest-free **1**. However, due to the slightly smaller cell parameters than guest-free **1**, some distortion of the linkers is still present as evidenced by the slight differences in carbonyl and DABCO shifts.

To investigate the effect of UV irradiation on the thermal properties, DSC measurements were performed on $1\supset AB_x$ samples with different loading volumes after 300 minutes UV irradiation (Figure 6, full data S30-34). For each loading level, the endothermic phase transition on the heating branch is significantly reduced and a small exothermic transition is subsequently observed. On the cooling branch, an exothermic phase transition is observed, as is the case for the non-irradiated samples. This behaviour was only observed in the first heating cycle; on the second cycle identical behaviour to the non-irradiated samples was observed on both the heating and cooling branches. Both XRPD and ^1H NMR of solvent-extracted AB showed that after the first heating cycle on irradiated $1\supset AB_x$, only *trans*-AB is present. This shows that thermal cycling of the $1\supset AB_x$ composites causes thermal reconversion of the occluded metastable *cis*-AB to the ground-state *trans*-AB isomer. Similar thermal reconversions have been reported by Grossman & coworkers for AB-containing systems where typically a single exotherm is observed for the thermal reversion of *cis*-AB to *trans*-AB.^{33,34,67} The magnitude of the observed exotherm is dependent on the enthalpy difference between *cis* and *trans* isomers which can be affected by local structure (confinement or intermolecular interaction), as well as inert structural units (such as polymer backbone or counter-ions), and has ranged from 12 – 173 J g⁻¹ depending on the type of composite and the functionalisation of azobenzene.^{21,28,68,69}

The expected magnitude of the *cis* to *trans* exotherm for $1\supset AB_{1,0}$ with a PSS of 40% *cis*-AB is 21 kJ mol⁻¹. This value was derived from an energy difference of 52.4 kJ mol⁻¹ between the *cis* and *trans* isomers based on the DFT-calculated energy difference for isolated molecules (S35), and taking into account the 40% PSS after 300 min irradiation. The DFT-calculated energy difference is similar to other theoretical studies,^{29,34,68} as well as experimental values for AB and related systems.^{32,70,71} However, on the heating step in the DSC measurement, an exotherm of only 1.8 kJ mol⁻¹ is observed. It is also noteworthy that the exotherm on the heating step is significantly reduced for all $1\supset AB_x$ samples studied, and the size of reduction is approximately linearly correlated to the proportion of AB molecules in the *cis* state (S34).

A possible explanation for the observed thermal behaviour is that the endothermic phase transition and exothermic *cis-trans* thermal reconversion on the first heating branch occur simultaneously which leads to cancelling of both features. To investigate this, the enthalpy associated with reconversion from the *cis* to *trans* isomers at the PSS was calculated for each loading level (S35 and S36). Additionally, the expected energy difference due to *cis-trans* thermal reconversion of $1\supset AB_{1,0}$, at different irradiation times, as a function of the proportion of *cis*-AB were calculated (full data shown in S36-39). The calculated enthalpies for *cis-trans* AB relaxation in $1\supset AB_{1,0}$, at the measured proportion of *cis*-AB, are very similar to the overall energy difference on the respective first heating branch (Figure 7a). This indicates that the energy differences are solely due to the thermal relaxation of *cis*-AB to *trans*-AB overlapping

with the endothermic phase transition. Furthermore, the calculated energy of *cis-trans* AB relaxation from the initial charging experiments on the $1\supset AB_x$ series is also similar to the reduction of energy in the first heating branch.

Additional DSC measurements showed the onset of the endothermic phase transition does not vary with the heating rate and remains very close to the temperature of the non-irradiated sample (S40-47). Conversely, the onset of the following exothermic transition linearly increases with the heating rate,

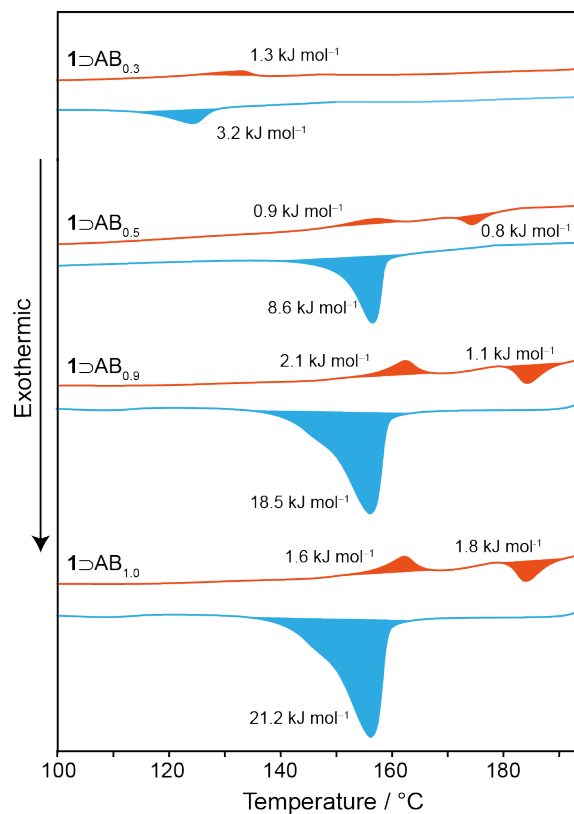


Figure 6. DSC cycles of irradiated $1\supset AB_x$, between 100 – 200 °C at a rate of 20 °C min⁻¹ where the first heating branches are in red, and the first cooling branches are in blue.

from 164–178 °C (S45-47). With faster heating rates, the energy of both transitions increases from 1.6 kJ mol⁻¹ up to 3.4 kJ mol⁻¹. This suggests the thermally-driven *cis-trans* reconversion can only happen after the endothermic phase transition. If *cis*-AB molecules switch to the *trans* isomer at the beginning of the endothermic phase transition, then the onset of the associated exotherm will not be visible.

Polymer-templated azobenzene STFs synthesised by Zhitomirsky *et al.* observed the *cis-trans* exotherm onset temperature at 120 °C,⁶⁷ whereas a 2-ethylhexyloxy modified liquid azobenzene reported by Masutani *et al.* has a considerably lower onset temperature (60 °C).³² The 2-ethylhexyloxy-modified azobenzene is close to the intrinsic temperature for reconversion because it is in the liquid state where steric effects are minimal. The higher onset temperature for the polymers reported by Zhitomirsky *et al.* show that the increased steric effects in the solid-state

can increase the temperature required for thermal reconversion. The onset of reconversion for $1\text{DAB}_{1.0}$ takes place at an even higher temperature (156 °C) than both of these examples, suggesting a greater degree of confinement, and that it is associated with the phase transition which is necessary to allow reconversion. The contraction of the framework and resultant host-guest interactions with AB appears to inhibit the backward relaxation and stabilises the *cis* isomer.

Unlike conventional STF materials, the full exotherm from the *cis-trans* reconversion is not fully observed in $1\text{DAB}_{1.0}$. However, for the irradiated sample, the overlap of the endothermic phase transition and the subsequent *cis-trans* thermal relaxation exotherm leads to a negligible net heat flow beyond the heat capacity of the composite on the first heating branch. However, at the end of the heating branch, the *cis-AB* molecules have thermally relaxed to *trans-AB*. The material then has the structural properties of non-irradiated $1\text{DAB}_{1.0}$ and therefore the exothermic phase change is observed on the cooling branch (S48). This means that over one full heating/cooling cycle there is a net energy output of 21.4 kJ mol⁻¹ or 28.9 J g⁻¹. This energy is indirectly derived from the stored energy in the metastable *cis* AB isomers. The total amount of energy stored increases with UV exposure time (S49) and under the irradiation conditions used in this work, within 120 minutes more than 85 % of the overall energy storage capacity is reached (corresponding to a PSS of 31%). It takes a further 180 minutes to reach the maximum PSS of 40%. As expected, the total thermal energy released from each irradiated 1DAB_x composite increases linearly with the quantity of *trans-AB* loaded into the **1** framework (Figure 7b).

The gravimetric energy density of 28.9 J g⁻¹ for $1\text{DAB}_{1.0}$ is modest compared to other STF architectures such as nanocarbon-templated Azo-STFs (200 J g⁻¹)³⁵ and polymer-templated Azo-STFs (90-104 J g⁻¹).^{67,72} Organic ss-PCMs can have energy densities in excess of 100 J g⁻¹ and organometallic ss-PCMs show energy densities in the range 60-165 J g⁻¹.⁶² However, one of the advantages of the MOF-based system is that solid-state charging to the PSS is readily achieved in powder form without the need to suspend in solution or cast into films. Indeed, a sample of $1\text{DAB}_{1.0}$ which was left in natural light for 30 days was measured periodically and reached PSS of 32% *cis-AB*, corresponding to an energy density of 24.0 J g⁻¹. Despite the lower gravimetric energy density, the gravimetric power density of $1\text{DAB}_{1.0}$ at a cooling rate of -20 °C min⁻¹ is 185 W Kg⁻¹ which is comparable to some of the higher energy density polymer templated azobenzene derivatives (100 - 250 W kg⁻¹). This is because, although the magnitude of the exotherm is lower, heat is released at a faster rate over a much smaller temperature range. This highlights the advantage of a crystalline system where phase changes are very well defined and happens at a precise temperature so that there is fast and controllable energy release.

Another important property of STFs is the duration for which energy can be stored under ambient conditions. For polymer and molecular azobenzene-based STFs, the half-life of the *cis*-isomeric state is typically on the order of tens

of hours in the solid-state, making these materials useful for *e.g.*, daily repeat cycle applications. For irradiated $1\text{DAB}_{1.0}$, no detectable *cis-trans* reconversion was observed over a period of 24 hours. To obtain an estimate of the half-life, an irradiated sample was kept in the dark at 25 °C for four months, with portions extracted and quantified at regular intervals. Over this time, the *cis* population changed from an initial value of 40% at the PSS to 38% (S50). This change is still negligible and only slightly larger than the error associated with the measurement. Assuming first-order kinetics and fitting to a monoexponential decay gives a half-life on the order of 4.5 years (S50). As already observed by ¹³C CPMAS NMR, the *cis-AB* molecules occluded in $1\text{DAB}_{1.0}$ are highly dynamic but the restricted reconversion to *trans-AB* suggests a strong steric effect where the framework imposes a large activation energy for the reconversion to the *trans* state. The confinement of the *cis* isomers within the pores largely inhibits spontaneous reconversion to the *trans* isomer at ambient temperature. The extremely long half-life observed for $1\text{DAB}_{1.0}$ offers clear potential for the development of confined photoswitches for long-term or seasonal energy storage.

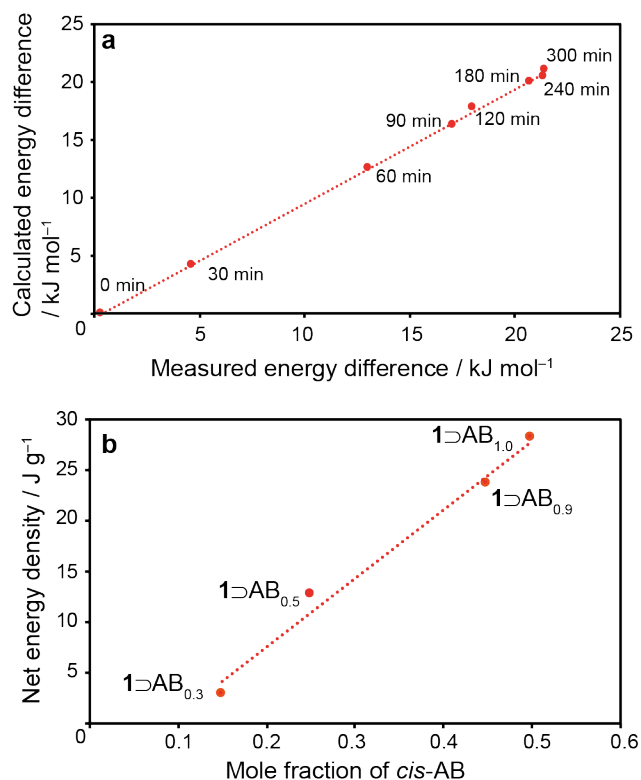


Figure 7. a) Measured enthalpy difference on the first heating branch of irradiated $1\text{DAB}_{1.0}$ compared with the calculated energy difference of *cis* to *trans* AB in $1\text{DAB}_{1.0}$ at based on the PSS different irradiation times. b) Net gravimetric energy density of 1DAB_x over a full heating cycle as a function of AB loading.

4. CONCLUSION

This work shows that MOFs incorporating confined photoswitches offer interesting possibilities for solid-state solar energy conversion and storage. The incorporation of

trans-AB within the pores of **1** leads to a guest-induced breathing effect and a reversible phase transition which gives the composite the properties a ss-PCM, albeit with limitations due to the loss of guest molecules from the pores above the phase transition temperature. The precise nature of the reversible phase transition has not been fully established but it may involve reorientation or rearrangement of the guest molecules and/or structural changes within the host framework. Irradiation with UV light converts occluded AB molecules to the metastable *cis* isomer with a maximum PSS of 40%. The contraction of the pores around the guest molecules stabilises the *cis* isomer, resulting in negligible reconversion over several months at ambient temperature. Thermal reconversion to the ground state *trans* isomer only occurs when the sample is heated above the phase transition temperature. For **1**⊃AB_{1.0}, the exothermic and endothermic enthalpies associated with the isomeric reconversion and the phase transition are comparable in magnitude and cancel each other, meaning only the exotherm is observed upon cooling. Therefore, over a full heating-cooling cycle, an overall thermal energy release is observed with a maximum value of 28.9 J g⁻¹ for **1**⊃AB_{1.0}.

The structural properties of **1**⊃AB_x composites have been characterised in detail by XRPD and solid-state NMR, and reveal a structure where the guest AB molecules are confined but remain highly mobile within the pores. This controlled confinement appears to be key to the ability of the photoswitches to isomerise in the solid state, yet remain in the metastable state for periods of several years. The strategy of controlled confinement of photoswitches within porous materials opens the way for further optimisation of similar materials to obtain higher energy density. One way is through using photoswitches which achieve a higher PSS but retain an appreciable isomeric energy difference, such as functionalised AB derivatives⁷³ or arylazopyrazoles⁷⁴ – although any steric limitations on the PSS in these materials must also be understood. Work by Schneeman & coworkers has also suggested that the onset temperatures and enthalpies of *np-lp* and *lp-np* phase transitions in the host framework can be modulated by doping with M^{II} (M = Co, Ni, Fe, Cu) transition metal ions⁵³ as well as completely exchanging the transition metal cations.^{56,75} Work is ongoing in our laboratory to explore these possibilities.

ASSOCIATED CONTENT

Supporting Information. Full thermal data and DSC cycles of **1**⊃AB_x and irradiated **1**⊃AB_x; Full details and methodology for DFT calculations; simulated ¹³C CPMAS spectra of **1** frameworks and *trans*-AB; Le Bail fitting profiles for **1**⊃AB_{1.0} and irradiated **1**⊃AB_{1.0}; synthetic considerations including XRPD plots and *trans*-AB loading level determination. Full ¹³C CPMAS NMR and ¹H NMR spectra of **1**⊃AB_{1.0} and **1**⊃AB_{1.0} at variable temperature and irradiation times; calculation of *cis-trans* relaxation energy for **1**⊃AB_{1.0} and half-life.

This material is available free of charge via the Internet at <http://pubs.acs.org>.

AUTHOR INFORMATION

Corresponding Author

John M. Griffin – Department of Chemistry, Lancaster University, Lancaster, LA1 4YB, UK; ORCID 0000-0002-8943-3835; Email j.griffin@lancaster.ac.uk

Author Contributions

The manuscript was written through contributions of all authors. All authors have given approval to the final version of the manuscript.

Notes

The authors declare no competing financial interest

ACKNOWLEDGMENT

We are grateful to the Leverhulme Trust (Research Project Grant Number RPG-2018-395) for funding this project. The UK 850 MHz solid-state NMR Facility used in this research was funded by EPSRC and BBSRC (contract reference PR140003), as well as the University of Warwick including via part funding through Birmingham Science City Advanced Materials Projects 1 and 2 supported by Advantage West Midlands (AWM) and the European Regional Development Fund (ERDF).

ABBREVIATIONS

AB, azobenzene; ss-PCM, solid-state phase change material; STF, solar thermal fuel.

REFERENCES

- Mofijur, M.; Mahlia, T. M. I.; Silitonga, A. S.; Ong, H. C.; Silakhoori, M.; Hasan, M. H.; Putra, N.; Ashrafur Rahman, S. M. Phase Change Materials (PCM) for Solar Energy Usages and Storage: An Overview. *Energies* **2019**, *12* (16), 1–20.
- Jiang, Y.; Liu, M.; Sun, Y. Review on the Development of High Temperature Phase Change Material Composites for Solar Thermal Energy Storage. *Sol. Energy Mater. Sol. Cells* **2019**, *203* (July), 110164.
- Yuan, K.; Shi, J.; Aftab, W.; Qin, M.; Usman, A.; Zhou, F.; Lv, Y.; Gao, S.; Zou, R. Engineering the Thermal Conductivity of Functional Phase-Change Materials for Heat Energy Conversion, Storage, and Utilization. *Adv. Funct. Mater.* **2020**, *30* (8), 1–31.
- Wuttig, M.; Raoux, S. The Science and Technology of Phase Change Materials. *Zeitschrift fur Anorg. und Allg. Chemie* **2012**, *638* (15), 2455–2465.
- Raj, C. R.; Suresh, S.; Bhavsar, R. R.; Singh, V. K. Recent Developments in Thermo-Physical Property Enhancement and Applications of Solid Solid Phase Change Materials: A Review. *J. Therm. Anal. Calorim.* **2020**, *139* (5), 3023–3049.
- Sundararajan, S.; Samui, A. B.; Kulkarni, P. S. Versatility of Polyethylene Glycol (PEG) in Designing Solid-Solid Phase Change Materials (PCMs) for Thermal Management and Their Application to Innovative Technologies. *J. Mater. Chem. A* **2017**, *5* (35), 18379–18396.
- Umair, M. M.; Zhang, Y.; Iqbal, K.; Zhang, S.; Tang, B. Novel Strategies and Supporting Materials Applied to Shape-Stabilize Organic Phase Change Materials for Thermal Energy storage—A Review. *Appl. Energy* **2019**, *235* (October 2018), 846–873.
- Prajapati, D. G.; Kandasubramanian, B. Biodegradable Polymeric Solid Framework-Based Organic Phase-Change Materials for Thermal Energy Storage. *Ind. Eng. Chem. Res.* **2019**, *58*, 10652–10677.
- Alkan, C.; Günther, E.; Hiebler, S.; Ensari, Ö. F.; Kahraman, D. Polyurethanes as Solid-Solid Phase Change Materials for Thermal Energy Storage. *Sol. Energy* **2012**, *86* (6), 1761–1769.
- Xi, P.; Xia, L.; Fei, P.; Zhang, D.; Cheng, B. Preparation and

- Performance of a Novel Thermoplastics Polyurethane Solid-Solid Phase Change Materials for Energy Storage. *Sol. Energy Mater. Sol. Cells* **2012**, *102*, 36–43.
- (11) Kanj, A. B.; Müller, K.; Heinke, L. Stimuli-Responsive Metal-Organic Frameworks with Photoswitchable Azobenzene Side Groups. *Macromol. Rapid Commun.* **2018**, *39*, 1700239–170023953.
- (12) Su, J. C.; Liu, P. S. A Novel Solid-Solid Phase Change Heat Storage Material with Polyurethane Block Copolymer Structure. *Energy Convers. Manag.* **2006**, *47* (18–19), 3185–3191.
- (13) Alva, G.; Lin, Y.; Fang, G. Synthesis and Characterization of Chain-Extended and Branched Polyurethane Copolymers as Form Stable Phase Change Materials for Solar Thermal Conversion Storage. *Sol. Energy Mater. Sol. Cells* **2018**, *186*, 14–28.
- (14) Du, X.; Wang, H.; Du, Z.; Cheng, X. Synthesis and Thermal Properties of Novel Solid-Solid Phase Change Materials with Comb-Polyurethane Block Copolymer Structure for Thermal Energy Storage. *Thermochim. Acta* **2017**, *651*, 58–64.
- (15) Chen, C.; Liu, W.; Wang, H.; Zhu, L. Synthesis and Characterization of Novel Solid-Solid Phase Change Materials with a Polyurethane Copolymer Structure for Thermal Energy Storage. *RSC Adv.* **2016**, *6* (105), 102997–103005.
- (16) Chen, C.; Chen, J.; Jia, Y.; Topham, P. D.; Wang, L. Binary Shape-Stabilized Phase Change Materials Based on Poly(ethylene Glycol)/polyurethane Composite with Dual-Phase Transition. *J. Mater. Sci.* **2018**, *53* (24), 16539–16556.
- (17) Sari, A.; Bicer, A.; Alkan, C. Thermal Energy Storage Properties of Polyethylene Glycol Grafted Styrenic Copolymer as Novel Solid-Solid Phase Change Materials. *Int. J. Energy Res.* **2020**, *44* (5), 3976–3989.
- (18) Sari, A.; Bicer, A.; Alkan, C. Thermal Energy Storage Characteristics of Poly(styrene-Co-Maleic Anhydride)-Graft-PEG as Polymeric Solid-Solid Phase Change Materials. *Sol. Energy Mater. Sol. Cells* **2017**, *161*, 219–225.
- (19) Peng, K.; Chen, C.; Pan, W.; Liu, W.; Wang, Z.; Zhu, L. Preparation and Properties of β -cyclodextrin/4,4'-Diphenylmethane Diisocyanate/polyethylene Glycol (β -CD/MDI/PEG) Crosslinking Copolymers as Polymeric Solid-Solid Phase Change Materials. *Sol. Energy Mater. Sol. Cells* **2016**, *145*, 238–247.
- (20) Sarier, N.; Arat, R.; Menciloglu, Y.; Onder, E.; Boz, E. C.; Oguz, O. Production of PEG Grafted PAN Copolymers and Their Electrospun Nanowires as Novel Thermal Energy Storage Materials. *Thermochim. Acta* **2016**, *643*, 83–93.
- (21) Dong, L.; Feng, Y.; Wang, L.; Feng, W. Azobenzene-Based Solar Thermal Fuels: Design, Properties, and Applications. *Chem. Soc. Rev.* **2018**, *47* (19), 7339–7368.
- (22) Kucharski, T. J.; Tian, Y.; Akbulatov, S.; Boulatov, R. Chemical Solutions for the Closed-Cycle Storage of Solar Energy. *Energy Environ. Sci.* **2011**, *4* (11), 4449–4472.
- (23) Ganguly, G.; Sultana, M.; Paul, A. Designing Efficient Solar-Thermal Fuels with [N₂N](9,10)Anthracene Cyclophanes: A Theoretical Perspective. *J. Phys. Chem. Lett.* **2018**, *9*, 328–334.
- (24) Gray, V.; Lennartson, A.; Ratanalert, P.; Börjesson, K.; Moth-Poulsen, K. Diaryl-Substituted Norbornadienes with Red-Shifted Absorption for Molecular Solar Thermal Energy Storage. *Chem. Commun.* **2014**, *50* (40), 5330–5332.
- (25) Dreos, A.; Wang, Z.; Udmark, J.; Ström, A.; Erhart, P.; Börjesson, K.; Nielsen, M. B.; Moth-Poulsen, K. Liquid Norbornadiene Photoswitches for Solar Energy Storage. *Adv. Energy Mater.* **2018**, *8* (18), 1–9.
- (26) Mansø, M.; Petersen, A. U.; Wang, Z.; Erhart, P.; Nielsen, M. B.; Moth-Poulsen, K. Molecular Solar Thermal Energy Storage in Photoswitch Oligomers Increases Energy Densities and Storage Times. *Nat. Commun.* **2018**, *9* (1), 1–7.
- (27) Wang, Z.; Roffey, A.; Losantos, R.; Lennartson, A.; Jevric, M.; Petersen, A. U.; Quant, M.; Dreos, A.; Wen, X.; Sampedro, D.; et al. Macroscopic Heat Release in a Molecular Solar Thermal Energy Storage System. *Energy Environ. Sci.* **2019**, *12* (1), 187–193.
- (28) Cho, E. N.; Zhitomirsky, D.; Han, G. G. D.; Liu, Y.; Grossman, J. C. Molecularly Engineered Azobenzene Derivatives for High Energy Density Solid-State Solar Thermal Fuels. *ACS Appl. Mater. Interfaces* **2017**, *9* (10), 8679–8687.
- (29) Durgun, E.; Grossman, J. C. Photoswitchable Molecular Rings for Solar-Thermal Energy Storage. *J. Phys. Chem. Lett.* **2013**, *4* (6), 854–860.
- (30) Jeong, S. P.; Renna, L. A.; Boyle, C. J.; Kwak, H. S.; Harder, E.; Damm, W.; Venkataraman, D. High Energy Density in Azobenzene-Based Materials for Photo-Thermal Batteries via Controlled Polymer Architecture and Polymer-Solvent Interactions. *Sci. Rep.* **2017**, *7* (1), 1–12.
- (31) Wu, S.; Butt, H. J. Solar-Thermal Energy Conversion and Storage Using Photoresponsive Azobenzene-Containing Polymers. *Macromol. Rapid Commun.* **2020**, *41* (1).
- (32) Masutani, K.; Morikawa, M. A.; Kimizuka, N. A Liquid Azobenzene Derivative as a Solvent-Free Solar Thermal Fuel. *Chem. Commun.* **2014**, *50* (99), 15803–15806.
- (33) Kolpak, A. M.; Grossman, J. C. Azobenzene-Functionalized Carbon Nanotubes as High-Energy Density Solar Thermal Fuels. *Nano Lett.* **2011**, *11*, 3156–3162.
- (34) Kucharski, T. J.; Ferralis, N.; Kolpak, A. M.; Zheng, J. O.; Nocera, D. G.; Grossman, J. C. Templated Assembly of Photoswitches Significantly Increases the Energy-Storage Capacity of Solar Thermal Fuels. *Nat. Chem.* **2014**, *6* (5), 441–447.
- (35) Han, G. G. D.; Deru, J. H.; Cho, E. N.; Grossman, J. C. Optically-Regulated Thermal Energy Storage in Diverse Organic Phase-Change Materials. *Chem. Commun.* **2018**, *54* (76), 10722–10725.
- (36) Schneemann, A.; Bon, V.; Schwedler, I.; Senkowska, I.; Kaskel, S.; Fischer, R. A. Flexible Metal-Organic Frameworks. *Chem. Soc. Rev.* **2014**, *43* (16), 6062–6096.
- (37) Grosch, J. S.; Paesani, F. Molecular-Level Characterization of the Breathing Behavior of the Jungle-Gym-Type DMOF-1 Metal-Organic Framework. *J. Am. Chem. Soc.* **2012**, *134* (9), 4207–4215.
- (38) Ha, H.; Kim, Y.; Kim, D.; Lee, J.; Song, Y.; Kim, S.; Park, M. H.; Kim, Y.; Kim, H.; Yoon, M.; et al. Effect of the Metal within Regioisomeric Paddle-Wheel-Type Metal-Organic Frameworks. *Chem. - A Eur. J.* **2019**, *25* (63), 14414–14420.
- (39) Keupp, J.; Schmid, R. Molecular Dynamics Simulations of the “Breathing” Phase Transformation of MOF Nanocrystallites. *Adv. Theory Simulations* **2019**, *2* (11), 1900117.
- (40) Uemura, K.; Yamasaki, Y.; Komagawa, Y.; Tanaka, K.; Kita, H. Two-Step Adsorption/Desorption on a Jungle-Gym-Type Porous Coordination Polymer. *Angew. Chemie Int. Ed.* **2007**, *46* (35), 6662–6665.
- (41) Yanai, N.; Uemura, T.; Inoue, M.; Matsuda, R.; Fukushima, T.; Tsujimoto, M.; Isoda, S.; Kitagawa, S. Guest-to-Host Transmission of Structural Changes for Stimuli-Responsive Adsorption Property. *J. Am. Chem. Soc.* **2012**, *134* (10), 4501–4504.
- (42) Walton, I. M.; Cox, J. M.; Coppin, J. A.; Linderman, C. M.; Patel, D. G.; Benedict, J. B. Photo-Responsive MOFs: Light-Induced Switching of Porous Single Crystals Containing a Photochromic Diarylethene. *Chem. Commun.* **2013**, *49* (73), 8012–8014.
- (43) Das, D.; Agarkar, H. Unexpected Nonresponsive Behavior of a Flexible Metal-Organic Framework under Conformational Changes of a Photoresponsive Guest Molecule. *ACS Omega* **2018**, *3* (7), 7630–7638.
- (44) Dybtsev, D. N.; Chun, H.; Kim, K. Rigid and Flexible: A Highly Porous Metal-Organic Framework with Unusual Guest-Dependent Dynamic Behavior. *Angew. Chemie - Int. Ed.* **2004**, *43* (38), 5033–5036.
- (45) Bennett, A. E.; Rienstra, C. M.; Auger, M.; Lakshmi, K. V.; Griffin, R. G. Heteronuclear Decoupling in Rotating Solids. *J.*

- Chem. Phys.* **1995**, *103* (16), 6951–6958.
- (46) BIELECKI, A.; BURUM, D. P. Temperature Dependence of ^{207}Pb MAS Spectra of Solid Lead Nitrate. An Accurate, Sensitive Thermometer for Variable-Temperature MAS. *J. Magn. Reson. Ser. A* **1995**, *116* (2), 215–220.
- (47) Segall, M. D.; Lindan, P. J. D.; Probert, M. J.; Pickard, C. J.; Hasnip, P. J.; Clark, S. J.; Payne, M. C. First-Principles Simulation: Ideas, Illustrations and the CASTEP Code. *J. Phys. Condens. Matter* **2002**, *14* (11), 2717–2744.
- (48) Pickard, C. J.; Mauri, F. All-Electron Magnetic Response with Pseudopotentials: NMR Chemical Shifts. *Phys. Rev. B* **2001**, *63* (24), 245101.
- (49) Burtch, N. C.; Torres-Knoop, A.; Foo, G. S.; Leisen, J.; Sievers, C.; Ensing, B.; Dubbeldam, D.; Walton, K. S. Understanding DABCO Nanorotor Dynamics in Isostructural Metal–Organic Frameworks. *J. Phys. Chem. Lett.* **2015**, *6* (5), 812–816.
- (50) Khudozhitkov, A. E.; Kolokolov, D. I.; Stepanov, A. G.; Bolotov, V. A.; Dybtsev, D. N. Metal-Cation-Independent Dynamics of Phenylene Ring in Microporous MOFs: A ^2H Solid-State NMR Study. *J. Phys. Chem. C* **2015**, *119* (50), 28038–28045.
- (51) Harada, J.; Ogawa, K. Invisible but Common Motion in Organic Crystals: A Pedal Motion in Stilbenes and Azobenzenes. *J. Am. Chem. Soc.* **2001**, *123* (44), 10884–10888.
- (52) Harada, J.; Ogawa, K.; Tomoda, S. Molecular Motion and Conformational Interconversion of Azobenzenes in Crystals as Studied by X-Ray Diffraction. *Acta Crystallogr. Sect. B* **1997**, *53* (4), 662–672.
- (53) Schneemann, A.; Rudolf, R.; Baxter, S. J.; Vervoorts, P.; Hante, I.; Khaletskaia, K.; Henke, S.; Kieslich, G.; Fischer, R. A. Flexibility Control in Alkyl Ether-Functionalized Pillared-Layered MOFs by a Cu/Zn Mixed Metal Approach. *Dalt. Trans.* **2019**, *48* (19), 6564–6570.
- (54) Henke, S.; Schneemann, A.; Fischer, R. A. Massive Anisotropic Thermal Expansion and Thermo-Responsive Breathing in Metal–Organic Frameworks Modulated by Linker Functionalization. *Adv. Funct. Mater.* **2013**, *23* (48), 5990–5996.
- (55) Schwedler, I.; Henke, S.; Wharmby, M. T.; Bajpe, S. R.; Cheetham, A. K.; Fischer, R. A. Mixed-Linker Solid Solutions of Functionalized Pillared-Layer MOFs – Adjusting Structural Flexibility, Gas Sorption, and Thermal Responsiveness. *Dalt. Trans.* **2016**, *45* (10), 4230–4241.
- (56) Schneemann, A.; Vervoorts, P.; Hante, I.; Tu, M.; Wannapaiboon, S.; Sternemann, C.; Paulus, M.; Wieland, D. C. F.; Henke, S.; Fischer, R. A. Different Breathing Mechanisms in Flexible Pillared-Layered Metal–Organic Frameworks: Impact of the Metal Center. *Chem. Mater.* **2018**, *30* (5), 1667–1676.
- (57) Nishioka, K.; Suura, N.; Ohno, K.; Maeda, T.; Shimizu, M. Development of Fe Base Phase Change Materials for High Temperature Using Solid–Solid Transformation. *ISIJ Int.* **2010**, *50* (9), 1240–1244.
- (58) Lu, D.; Di, Y.; Dou, J. Crystal Structures and Solid–Solid Phase Transitions on Phase Change Materials $(1-\text{C}_n\text{H}_{2n+1}\text{NH}_3)_2\text{CuCl}_4(\text{s})$ ($n=10$ and 11). *Sol. Energy Mater. Sol. Cells* **2013**, *114*, 1–8.
- (59) Warke, I. J.; Patil, K. J.; Terdale, S. S. Thermophysical Properties of Aqueous Solutions of Tetraalkylphosphonium Based Ionic Liquids at Different Temperatures and Atmospheric Pressure. *J. Chem. Thermodyn.* **2016**, *93*, 101–114.
- (60) Lu, D. F.; Di, Y.-Y.; Tan, Z. C.; Dou, J. M. Low-Temperature Heat Capacities, and Thermodynamic Properties of Solid–solid Phase Change Material bis(1-Octylammonium) Tetrachlorocuprate. *J. Therm. Anal. Calorim.* **2013**, *111* (1), 213–218.
- (61) Whitman, C. A.; Johnson, M. B.; White, M. A. Characterization of Thermal Performance of a Solid–solid Phase Change Material, Di-N-Hexylammonium Bromide, for Potential Integration in Building Materials. *Thermochim. Acta* **2012**, *531*, 54–59.
- (62) Fallahi, A.; Guldentops, G.; Tao, M.; Granados-Focil, S.; Van Dessel, S. Review on Solid–Solid Phase Change Materials for Thermal Energy Storage: Molecular Structure and Thermal Properties. *Appl. Therm. Eng.* **2017**, *127*, 1427–1441.
- (63) Li, W.; Zhang, D.; Zhang, T.; Wang, T.; Ruan, D.; Xing, D.; Li, H. Study of Solid–solid Phase Change of $(\text{N}-\text{C}_n\text{H}_{2n+1}\text{NH}_3)_2\text{MCl}_4$ for Thermal Energy Storage. *Thermochim. Acta* **1999**, *326* (1), 183–186.
- (64) He, D.-H.; Di, Y.-Y.; Tan, Z.-C.; Yi, F.-F.; Dan, W.-Y.; Liu, Y.-P. Crystal Structures and Thermochemistry on Phase Change Materials $(\text{N}-\text{C}_n\text{H}_{2n+1}\text{NH}_3)_2\text{CuCl}_4(\text{s})$ ($n=14$ and 15). *Sol. Energy Mater. Sol. Cells* **2011**, *95* (10), 2897–2906.
- (65) He, D.-H.; Di, Y.-Y.; Yao, Y.; Liu, Y.-P.; Dan, W.-Y. Crystal Structure, Low-Temperature Heat Capacities, and Thermodynamic Properties of Bis(dodecylammonium) Tetrachlorocuprate $(\text{C}_{12}\text{H}_{28}\text{N})_2\text{CuCl}_4(\text{s})$. *J. Chem. Eng. Data* **2010**, *55* (12), 5739–5744.
- (66) Beharry, A. A.; Woolley, G. A. Azobenzene Photoswitches for Biomolecules. *Chem. Soc. Rev.* **2011**, *40* (8), 4422–4437.
- (67) Zhitomirsky, D.; Cho, E.; Grossman, J. C. Solid-State Solar Thermal Fuels for Heat Release Applications. *Adv. Energy Mater.* **2016**, *6* (6), 1502006.
- (68) Han, G. D.; Park, S. S.; Liu, Y.; Zhitomirsky, D.; Cho, E.; Dincă, M.; Grossman, J. C. Photon Energy Storage Materials with High Energy Densities Based on Diacetylene–azobenzene Derivatives. *J. Mater. Chem. A* **2016**, *4* (41), 16157–16165.
- (69) Saydjari, A. K.; Weis, P.; Wu, S. Spanning the Solar Spectrum: Azopolymer Solar Thermal Fuels for Simultaneous UV and Visible Light Storage. *Adv. Energy Mater.* **2017**, *7* (3), 7–10.
- (70) Dias, A. R.; Minas Da Piedade, M. E.; Martinho Simões, J. A.; Simoni, J. A.; Teixeira, C.; Diogo, H. P.; Meng-Yan, Y.; Pilcher, G. Enthalpies of Formation of Cis-Azobenzene and Trans-Azobenzene. *J. Chem. Thermodyn.* **1992**, *24* (4), 439–447.
- (71) Cammenga, H. K.; Emel'yanenko, V. N.; Verevkin, S. P. Re-Investigation and Data Assessment of the Isomerization and $2,2'$ -Cyclization of Stilbenes and Azobenzenes. *Ind. Eng. Chem. Res.* **2009**, *48* (22), 10120–10128.
- (72) Zhitomirsky, D.; Grossman, J. C. Conformal Electroplating of Azobenzene-Based Solar Thermal Fuels onto Large-Area and Fiber Geometries. *ACS Appl. Mater. Interfaces* **2016**, *8* (39), 26319–26325.
- (73) Beharry, A. A.; Sadovski, O.; Woolley, G. A. Azobenzene Photoswitching without Ultraviolet Light. *J. Am. Chem. Soc.* **2011**, *133* (49), 19684–19687.
- (74) Weston, C. E.; Richardson, R. D.; Haycock, P. R.; White, A. J. P.; Fuchter, M. J. Arylazopyrazoles: Azoheteroarene Photoswitches Offering Quantitative Isomerization and Long Thermal Half-Lives. *J. Am. Chem. Soc.* **2014**, *136* (34), 11878–11881.
- (75) Klein, N.; Hoffmann, H. C.; Cadiou, A.; Getzschmann, J.; Lohe, M. R.; Paasch, S.; Heydenreich, T.; Adil, K.; Senkovska, I.; Brunner, E.; et al. Structural Flexibility and Intrinsic Dynamics in the $\text{M}_2(2,6\text{-ndc})_2(\text{dabco})$ ($\text{M} = \text{Ni}, \text{Cu}, \text{Co}, \text{Zn}$) Metal–organic Frameworks. *J. Mater. Chem.* **2012**, *22* (20), 10303–10312.

TOC graphic

